# Coseismic slip and afterslip of the 2015 $M_w$ 8.3 Illapel (Chile) earthquake determined from continuous GPS data

**Mahesh N. Shrivastava[1,2], Gabriel González[1,2], Marcos Moreno[3], Mohamed Chlieh[4], Pablo Salazar[1,2], C. D. Reddy[5], Juan Carlos Báez[6], Gonzalo Yáñez[1,7], Juan González[1,2], and Juan Carlos de la Llera[1,7]**

[1]National Research Center for Integrated Natural Disaster Management, Santiago, Chile, [2]Departamento de Ciencias Geológicas, Universidad Católica del Norte, Antofagasta, Chile, [3]Helmholtz Centre Potsdam GFZ German Research Centre for Geosciences, Potsdam, Germany, [4]Geoazur, Université de Nice Sophia-Antipolis, OCA, IRD, CNRS, Valbonne, France, [5]Indian Institute of Geomagnetism, Mumbai, India, [6]Centro Sismológico Nacional, Universidad de Chile, Santiago, Chile, [7]Escuela de Ingeniería, Pontificia, Universidad Católica de Chile, Santiago, Chile

**Abstract** We analyzed the coseismic and early postseismic deformation of the 2015, $M_w$ 8.3 Illapel earthquake by inverting 13 continuous GPS time series. The seismic rupture concentrated in a shallow ($<20$ km depth) and 100 km long asperity, which slipped up to 8 m, releasing a seismic moment of $3.6 \times 10^{21}$ Nm ($M_w = 8.3$). After 43 days, postseismic afterslip encompassed the coseismic rupture. Afterslip concentrated in two main patches of 0.50 m between 20 and 40 km depth along the northern and southern ends of the rupture, partially overlapping the coseismic slip. Afterslip and aftershocks confined to region of positive Coulomb stress change, promoted by the coseismic slip. The early postseismic afterslip was accommodated ~53% aseismically and ~47% seismically by aftershocks. The Illapel earthquake rupture is confined by two low interseismic coupling zones, which coincide with two major features of the subducting Nazca Plate, the Challenger Fault Zone and Juan Fernandez Ridge.

## 1. Introduction

Subduction zone earthquakes (with $M_w \geq 8$) normally break across the entire width of the seismogenic zone in the downdip direction, but maximum slip is in most cases concentrated in a limited number of seismic asperities [*Lay et al.*, 1982; *Chlieh et al.*, 2008]. The distribution of locking and creeping regions suggests that the subduction interface is extremely heterogeneous [*McCaffrey*, 2002; *Chlieh et al.*, 2011; *Loveless and Meade*, 2011; *Métois et al.*, 2012; *Moreno et al.*, 2012; *Chlieh et al.*, 2014; *Béjar-Pizarro et al.*, 2013; *Métois et al.*, 2016; *Loveless and Meade*, 2016] and composed of a complex assemblage of various patches of seismic and aseismic behavior as well as patches exhibiting dual behavior capable of both slipping aseismically and during seismic ruptures. Hence, reliable identification of the seismic and aseismic slip during and after large megathrust earthquakes provides important insights into the mechanical basis of strain/stress buildup and release at subduction zones.

On 16 September 2015, a great subduction earthquake ($M_w$ 8.3) occurred off the coast of central Chile, with a hypocenter near the city of Illapel (71.55°W, 31.55°S, depth = 29 km, GEOFOrschungsNetz) directly beneath the coastline (Figure 1). Along this subduction segment, the Nazca Plate is subducting beneath the South American Plate with a convergence rate of ~66 mm/yr [*Altamimi et al.*, 2011]. The Illapel earthquake ruptured a segment of approximately 200 km long between the rupture regions of the $M_s$ 8.3, 1922 Atacama earthquake [*Beck et al.*, 1998] and the $M_s$ 8.4, 1906 Valparaiso earthquake [*Okal*, 2005]. The greatest previous megathrust event in this region occurred in 1730 ($M_s > 8.5$) and affected an approximately 500 km long segment that not only included the 2015 Illapel rupture region but extended southward to the 2010 Maule rupture region [*Udías et al.*, 2012; *Lomnitz*, 2004; *Métois et al.*, 2012]. The region of the Illapel earthquake seems to have been shattered by two previous moderates in magnitude subduction earthquakes in 1943 ($M_s$ 7.9) [*Beck et al.*, 1998] and 1880 ($M_s$ 7.5) [*Lomnitz*, 2004].

A first-order inspection showed that the rupture region of the 2015 Illapel earthquake was laterally confined by two prominent tectonic features of the Nazca seafloor: the Challenger Fault Zone (CFZ) in the north and the Juan Fernandez Ridge (JFR) in the south (Figure 1). Historical seismicity indicates that the CFZ acted as sharp boundary for the propagation of large subduction earthquakes ($M_s$ 8.3, 1922 Atacama and $M_s > 8.5$, 1730 earthquakes). According to interseismic geodetic models, the segment that ruptured during the
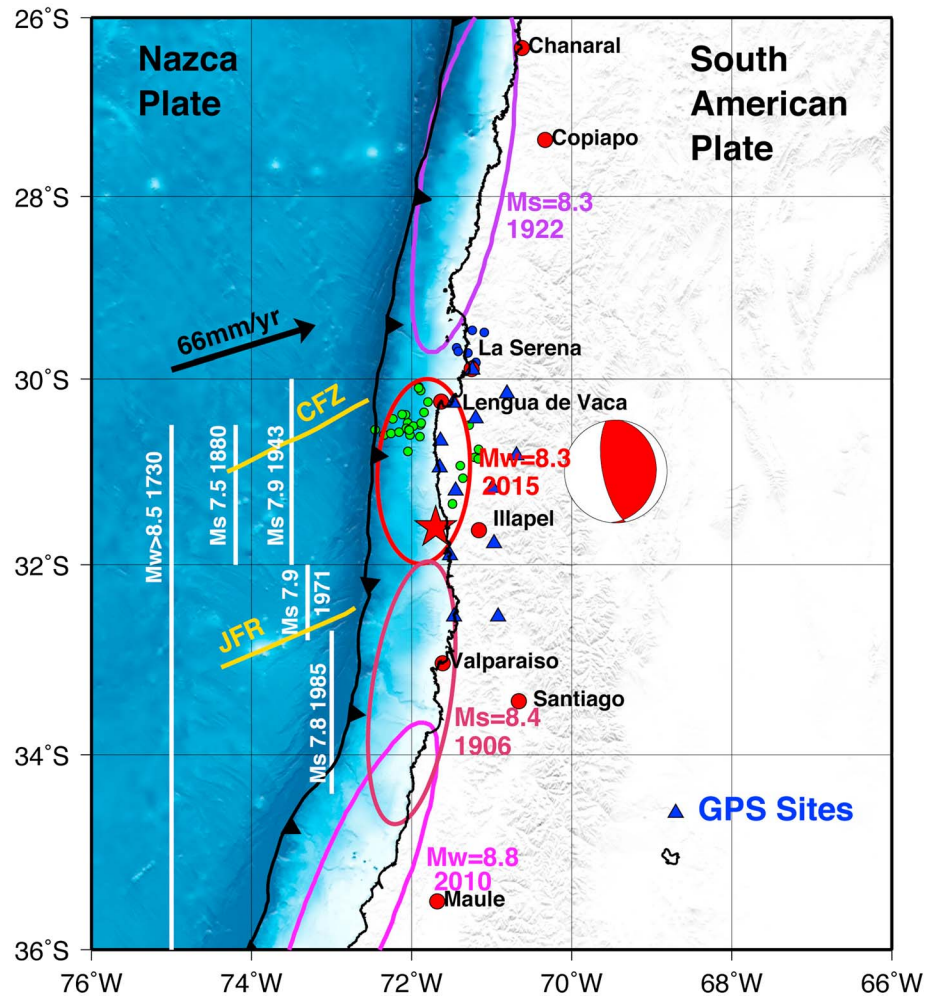
**Figure 1.** Seismo-tectonic features of the Central Chile subduction zone. The black barbed line shows the trench location that delimits the Nazca and South American Plates, which converge at 66 mm/yr. The yellow lines show the CFZ and the JFR [*Müller et al.*, 1997]. The ellipses indicate the location of large ($M_S$ 7.5) and great (>8.5) historical subduction earthquakes [*Beck et al.*, 1998; *Comte et al.*, 1986; *Lomintz et al.*, 2004]. The white lines indicate approximate rupture length of historical large (1880 and 1943) and great (1730) events. The 2015 rupture region (red ellipse) is shown with its epicenter (red star) and associated focal mechanism obtained from the global CMT (http://earthquake.usgs.gov/earthquakes/eventpage/us20003k7a#scientific_moment-tensor). The green dots show the seismic swarms that occurred in 1997 and 1998, and the blue dots show the seismic cluster near Coquimbo [*Lemoine et al.*, 2001] and La Serena in August 2015.

Illapel earthquake was preseismically more highly coupled than adjacent regions [*Métois et al.*, 2012, 2016; *Tilmann et al.*, 2016], in a similar fashion that characterized previously well-monitored megathrust earthquakes in Chile [*Moreno et al.*, 2010; *Métois et al.*, 2012; *Schurr et al.*, 2014]. Interestingly, the northern region of the 2015 Illapel rupture had experienced significant seismic swarm in 1997 [*Lemoine et al.*, 2001] and clusters of seismicity in 2015 (see in Figure 1).

In order to better understand the mechanical properties of the subduction megathrust segment activated during the 2015 Illapel earthquake, we studied the coseismic slip pattern and its associated early 43 day postseismic slip using continuous Global Positioning System (cGPS) observations and aftershock relocation. Our main aim was to map the fault slip regions that were activated during this earthquake and in the early relaxation period to better understand how frictional properties at the plate interface evolved.

## 2. GPS Data and Processing

We processed cGPS data of 13 permanent sites (Bahía de Tongoy (BTON), Combarbalá (CMBA), Ovalle (OVLL), Canela Baja (CNBA), La Serena (LSCH), Cerro Negro (CERN), Caleta El Maiten (EMAT), Los Vilos (LVIL), Tololo

(TOLO), Pedregal (PEDR), Parque Fray Jorge (PFRJ), Salamanca (SLMC), and Zapallar (ZAPA)) around the rupture region of the 2015 Illapel earthquake from 230 to 302 day of year 2016. GPS data of the sites BTON (275–302), OVLL (275–302), TOLO (271–288), CERN (273–302), and EMAT (241–273) were not available (see Figures S6 and S8 in the supporting information). These GPS sites were installed in the early 2000s by the Chilean-French International Laboratory (LIA) Montessus de Ballore and are now being managed in collaboration with the Centro Sismológico Nacional (CSN). We used coseismic displacement (east-north-up (ENU)) components from time series to model the coseismic slip and afterslip distributions, respectively. During coseismic displacements, we have taken the position difference in ENU component for the all the GPS sites, but one GPS site EMAT that was not working on day of the earthquake. Therefore, we have extrapolated the interseismic phase up to the earthquake day. After the modeling of the afterslip, we obtained the modeled ENU component of the EMAT GPS site. We used the extrapolated interseismic and modeled ENU component to model the coseismic slip. We estimated the daily positions of GPS sites with fiducial sites by using GAMIT/GLOBK postprocessing software [*King and Bock*, 2002; *Herring et al.*, 2002] in two steps. In the first step, daily loose GAMIT results are acquired, which accounted for error contributions due to signal delay by the atmosphere, orbital accuracy, antenna phase center variations, signal multipath, and satellite as well as receiver clock errors. Ambiguity-free and ambiguity-fixed solutions were executed with ionosphere-free linear combinations to account for carrier phase ambiguity and signal delay due to ionosphere. We included International Global Navigation Satellite Systems (GNSS) Service IGS tables for the corrected position of the phase centers of antennas and estimated the tropospheric vertical delay parameter per station every 3 h. The horizontal (east and north) and vertical (up) components relative to the position vectors are precise within 2–3 and 4–5 mm, respectively. Precise orbits and Earth rotation parameters obtained from the International GNSS Service (IGS) for Geodynamics [*Dow et al.*, 2009] were used. The GPS sites were estimated daily and independently by weighted least squares technique. In the second step, loosely constrained daily solutions from global tracking IGS sites were combined with daily solutions obtained from GAMIT, resulting in loosely constrained positions for the entire survey span. These combined solutions were passed through a Kalman filter via GLOBK software in a regional stabilization process [*Herring et al.*, 2002] to estimate network adjusted site coordinates. *Vigny et al.* [2011] identified the GPS sites Savanes de Karouabo (KOUR) in French Guyana; Santa Barbara (BRAZ), Eusébio (BRFT), and Cachoeira Paulista (CHPI) in Brazil, and Río Grande (RIO2) in Patagonia, and Galápagos (GLPS) on the Nazca Plate were unaffected from the Maule earthquake in 2010. These unaffected GPS sites GLPS, KOUR, BRAZ, and RIO2 were used in the analysis as constraints according to the reported value of reference station positions with standard errors provided by IGS. International Terrestrial Reference Frame (ITRF) 2008 was realized through GLORG by using local generated H-files. This stabilization strategy defines a reference frame by minimizing, in the least squares sense, the departure from the a priori data determined in the ITRF2008 [*Altamimi et al.*, 2011]. For correct coseismic displacement, we discarded remaining GPS data for each site on 16 September 2015, after the earthquake and took the position difference between the day before and after the Illapel earthquake. The coseismic GPS displacements are provided in Table S1 in the supporting information, and repeatability with error is provided in Figure S6.

## 3. Modeling Setup

We inverted the GPS time series using the Principal Component Analysis-based Inversion Method (PCAIM) [*Kositsky and Avouac*, 2010; *Perfettini et al.*, 2010]. We used the subduction model Slab1.0 described in *Hayes et al.* [2012] to build the megathrust geometry. The seismogenic zone is in this region around 50 km and most of the aseismic slip takes place in the downdip part of the seismogenic zone. So we extended fault from 28.2°S to 32.2°S along-strike and from the trench axis to a depth of about 60 km along-dip (see Figures 2a and 3a). The slab is meshed by 456 rectangular elements with an average area of 137 km$^2$ and implanted in a homogeneous half-space with a shear modulus of 35 GPa and Poisson's ratio 0.25 [*Haberland et al.*, 2009]. The slip on the rectangular elements was regularized by using a Laplacian operator to smoothen the final slip distribution on the fault rooted in the L-curve [*Hansen*, 1992; *Hansen and O'Leary*, 1993]. Boundary conditions were implemented at the borders of the slab fault along the trench to constrain the slip to zero, while other boundaries of the fault were not constrained. The displacements were decomposed into principal components that were individually modeled before to reconstruct the final seismic source and afterslip models [*Perfettini and Avouac*, 2014; *Perfettini et al.*, 2010]. A checkerboard test was performed to estimate the resolution power of the GPS network (Figure S1). It shows that our modeling has good
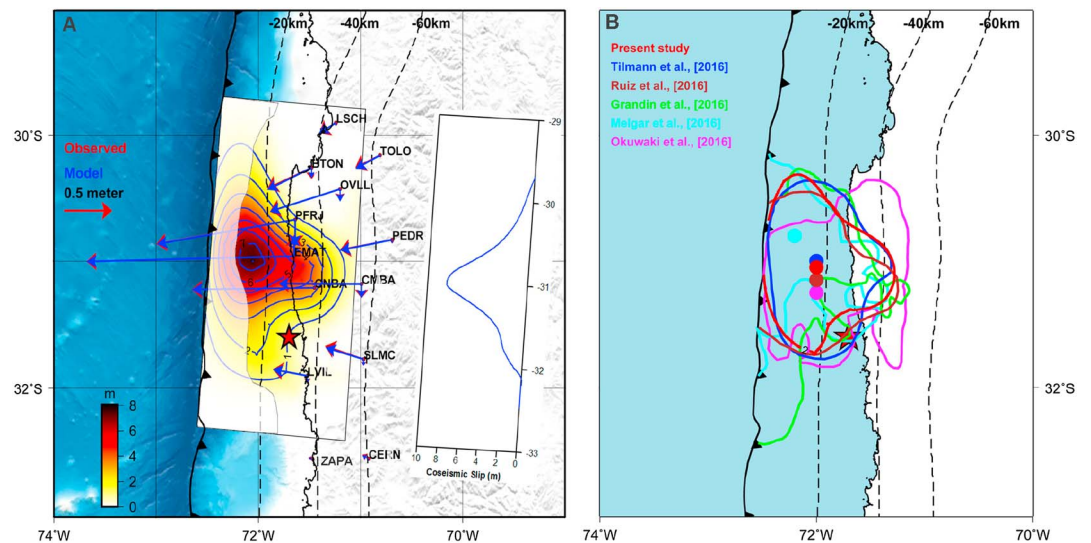
**Figure 2.** (a) Coseismic slip (1 m contour) derived from the modeling of continuous GPS data. The red and blue arrows show the observed and modeled GPS displacements, respectively. Slab megathrust contours (every 20 km depth) are taken from *Hayes et al.* [2012]. The inset shows the latitudinal variation of the seismic moment released during the 2015 event, which shows a Gaussian shape of about 200 km length and centered at latitude 31°S. The grey color shaded region depicts the poor resolution. (b) The coseismic slip distributions compared with published coseismic slip with contour 2 m as well as the maximum slip regions with closed dots. The contour and closed dotted color correspond to the author name mentioned in the figure.

resolution from 15 km updip to the 60 km downdip in the region of maximum coseismic slip and it changes along the strike. The boundary of poor and good resolution is shown by grey color line in Figure S1b. The grey color shaded region depicts the poor resolution on the coseismic slip in the Figure 2a and on the afterslip in the Figure 3a. Smoothing parameters $\gamma$ with red chi-square for coseismic slip and afterslip are provided in Figure S9.
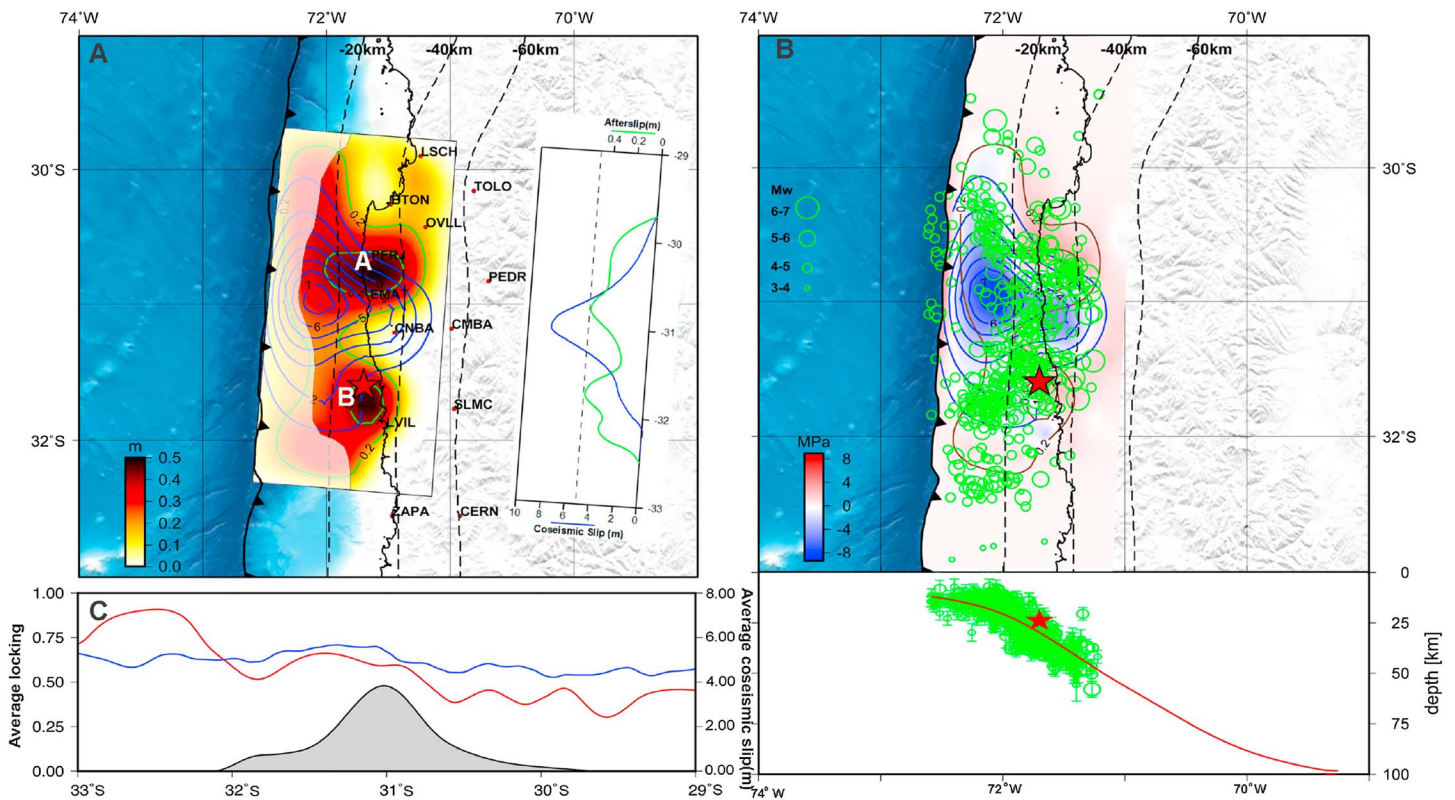
### 3.1. Coseismic GPS Data and Seismic Source

All the GPS sites recorded decimeters to meters of horizontal displacement toward the trenchward direction (Figure 2a), with an increasing gradient toward the coastline. A maximum horizontal coseismic displacement of 2.13 m was recorded at the GPS site EMAT, located close to the coastline at latitude 31°S. At GPS sites EMAT and CNBA, uplift of about 25 cm was recorded, attesting that some significant coseismic slip did occur below these two GPS sites. All other GPS sites experienced vertical subsidence of few millimeters to centimeters, suggesting an offshore coseismic slip.

By inverting the GPS displacements, we found that coseismic slip was concentrated in a single patch about 100 km wide at a latitude of 31°S. A peak in seismic slip of 8 m was reached at a latitude of 31°S at about 17 km depth (Figure 2a). At this same latitude, coseismic slip partially propagated below the coastline in a region well resolved by the GPS network. Our slip distribution yields a geodetic seismic moment of $M_o = 3.6 \times 10^{21}$ Nm, equivalent to an $M_w = 8.3$ earthquake. See Table S1 for more details of the coseismic displacements and prediction of the model.

### 3.2. Postseismic GPS Time Series and Afterslip Distribution

Postseismic signals appeared very clearly in all GPS time series, showing a westward motion that rapidly decayed with increasing time and increasing distance from the source region (Figures S6 and S8). Early postseismic deformation is generally attributed to afterslip and used to infer the frictional properties of the plate interface [*Hsu et al.*, 2006; *Perfettini and Avouac*, 2004]. Therefore, we suppose that the early near-field postseismic deformation of the Illapel earthquake can be modeled only by afterslip, neglecting viscous mantle effects that may impact the long-term postseismic relaxation. We inverted the GPS time series during 43 days of postseismic relaxation following the 2015 Illapel main shock using the PCAIM code (http://www.tectonics.caltech.edu/resources/pcaim). This code generates daily afterslip solutions, and the model fits fairly well with the GPS time series (see Figure S8). In Figure 3a, we report the 43 days cumulative postseismic afterslip

**Figure 3.** (a) Postseismic afterslip (20 cm contours, green) derived from the modeling of 43 days of continuous postseismic GPS data. After 43 days, most of the afterslip occurred around the coseismic source with two peaks of afterslip reaching 50 cm between 20 and 40 km depths. The inset shows the along-strike variation of the afterslip (green, top scale) compared with the coseismic slip (blue in bottom scale) shown in the inset of Figure 2a. The white color A and B letters show the patches of the maximum afterslip. The grey color shaded region depicts the poor resolution. (b) Coulomb stress change with aftershocks. The green open circles show the aftershocks. The aftershocks $M_W > 6.0$ are shown as a blue open star; the closed red star shows the epicenter of the Illapel earthquake. The coseismic slip contour is shown in blue and the afterslip in dark brown color. The subplot represents the aftershocks of the Illapel earthquake along the megathrust. The blue color open star represents aftershocks $M_W > 6.0$, and the red color closed star represents the epicenter of the Illapel earthquake. (c) Pictorial correlation of published interseismic coupling and coseismic slip modeled in the present study. The average locking and average coseismic slip are shown in Figure 3c. The grey color area plot shows the average coseismic slip, and the red color and blue color lines show the locking model of *Métois et al.* [2016] and *Tilmann et al.* [2016], respectively.

distribution. Postseismic afterslip appears to surround and partially overlap the 2015 coseismic rupture region. Our model shows two major afterslip zones: a large region located south of the Lengua de Vaca Peninsula (Patch A) and another one located near the epicenter (Patch B). These two patches of higher afterslip (~0.50 m) appear at 20 to 40 km depth, just to the northeast and southeast of the single patch of higher coseismic slip (see Figure S4). After 43 days, we estimated a cumulative postseismic moment of $4.2 \times 10^{20}$ Nm, which is equivalent to ~12% of the 2015 coseismic moment. The evolution of afterslip patches started to appear during the first 10 days and was enhancing with time (Figure S7). See Table S2 for more details of the cumulative postseismic displacements and prediction of the model. The modeled and observed GPS site positions are provided in Figure S8.

## 4. Discussion

### 4.1. Seismic Source Characteristics

The seismic source of the 2015 Illapel earthquake shows that most of the coseismic slip occurred around a shallow (<20 km depth) seismic asperity ~100 km wide along-strike that slipped up to 8 m. A substantial coseismic slip (3–5 m) propagated between 20 and 40 km depth in the central portion of the rupture zone, right below the coastline. A previous coseismic slip model obtained by *Ruiz et al.* [2016], using geodetic data, has a good spatial correlation with our coseismic slip distribution, showing similar location of maximum coseismic slip and distribution of the 2 m slip contour. Other published coseismic models based on
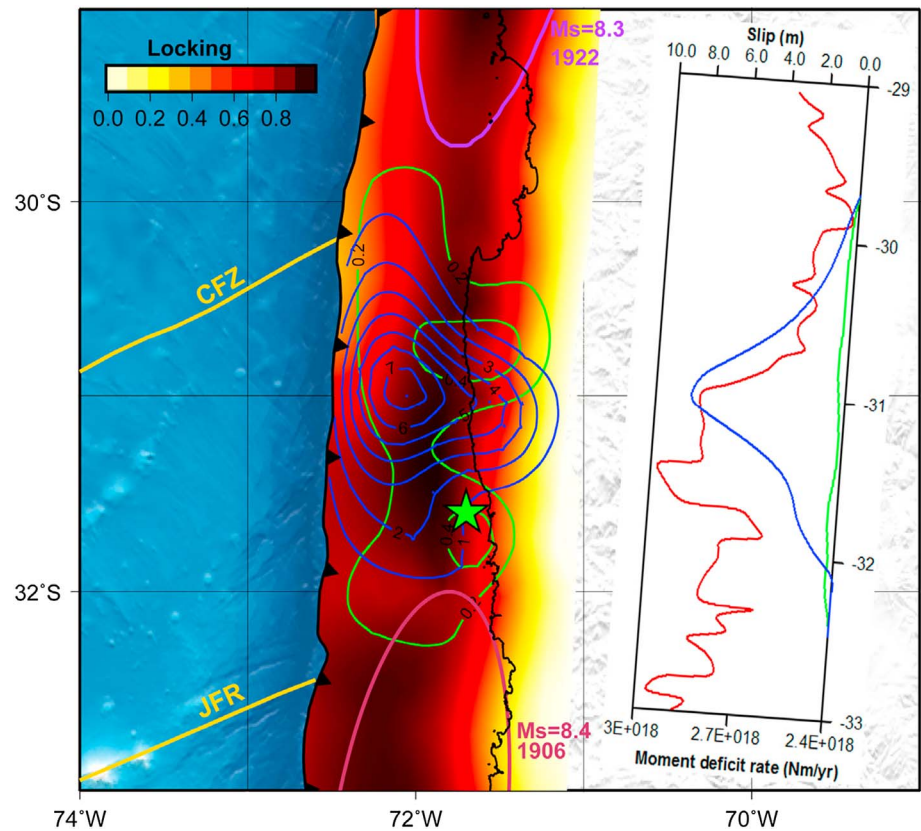
**Figure 4.** Interseismic coupling model [*Tilmann et al.*, 2016] derived from interseismic GPS data collected [*Vigny et al.*, 2009; *Métois et al.*, 2012, 2014] before the 2015 Illapel earthquake. The blue and green lines refer to the coseismic slip of Figure 2a and the postseismic afterslip of Figure 3a, respectively. The CFZ and the JFR delimit the rupture region of the 2015 Illapel earthquake. The inset shows the along-strike variation of the moment deficit rate (red line and bottom scale) compared with the coseismic moment released (blue line and top scale) and with the afterslip moment released (green line and top scale).

teleseismic, GPS, interferometric synthetic aperture radar (InSAR), and tsunami data [e.g., *Okuwaki et al.*, 2016; *Grandin et al.*, 2016; *Tilmann et al.*, 2016; *Heidarzadeh et al.*, 2016; *Li et al.*, 2016; *Lee et al.*, 2016; *Ruiz et al.*, 2016; *Zhang et al.*, 2016] are also in agreement with our results (Figure 2b). *Melgar et al.* [2016] used high-rate GPS, strong motion, InSAR, and tide gauge to suggest that slip may have be initiated from downdip and propagated into the shallow dip region, finding a maximum slip concentration in a shallow region. According to previous ISC models proposed by several authors [*Métois et al.*, 2014, 2016; *Tilmann et al.*, 2016], the 2015 coseismic slip of the Illapel earthquake occurred in a relatively highly coupled region with respect to the surrounding interface region (Figure 4). We noticed that the ISC was lower where the CFZ and JFR entered into subduction (Figure 4), suggesting that these features may induce a local decrease of strain accumulation, acting as barriers to the 2015 seismic rupture propagation. It has been suggested that subducting seamounts produce small earthquakes and regions characterized by aseismic creep [*Wang and Bilek*, 2011]. In these types of settings, the rupture process is dominated by a complex pattern of slipping regions instead a single fault plane [*Bilek et al.*, 2003] and by high fluid pressure that drastically reduces the locking at the plate interface [*Mochizuki et al.*, 2008; *Moreno et al.*, 2014; *Henstock et al.*, 2016]. In contrast, it has been suggested that subducting seamounts can nucleate great subduction earthquakes [*Scholz and Small*, 1997; *Duan*, 2012]. *Lange et al.* [2016] have mapped the subducting seamounts of JFR in the southern boundary of the Illapel earthquake. The locking models of *Tilmann et al.* [2016] and *Métois et al.* [2016] show that the subducting JFR was a region of relative low locking as compared with the surrounding regions. It indicates that the subduction of small seamounts plays a key role to reduce the ISC and to stop the Illapel rupture in the JFR.

### 4.2. Afterslip Characteristics

Forty-three days after the main shock, the cumulative postseismic afterslip model showed that two patches slipped up to 0.50 m, just north and south of the deepest part of the 2015 coseismic slipped region (~20–40 km depth). The evolution of these two patches appeared during the first 10 days after the main shock (Figure S7). The afterslip distribution occurred in the region adjacent to the higher coseismic slip region (Figure 3a). Figure 3a shows that the patch (A) partially overlaps with a zone of 1 to 4 m contour of coseismic slip in the northeast. *Johnson et al.* [2012] reported a similar observation in the Tohoku-oki earthquake 2011. In addition, they suggested that some patches have both velocity weakening and strengthening properties. In order to test if the observation is a real or an artifact of the model, we modeled afterslip by using the contour of 3 m coseismic slip as locked. Under this condition, we noticed that the observed and modeled displacement did not fit well (Figures S10 and S11). Therefore, we conclude that the situation of overlapping is an actual observation. We interpreted that this observation may be due to fluid migration downdip of the maximum coseismic slip zone. According to the coseismic slip contours, this region is characterized by extensional strain parallel to the interplate contact in the updip direction. This type of setting favors dilatancy and fluid migration.

We computed the Coulomb stress change (CSC) (see Figure S2) induced by the coseismic slip shown in Figure 3b. It is comparable with high and low regions of CSC computed by *Tilmann et al.* [2016]. Most of the afterslip and aftershocks occurred in the region of positive CSC. For better understanding of the seismic and aseismic slip in the early postseismic period, we relocated 509 aftershocks with a minimum of $M_w > 3.7$ during the 43 days from the seismic waveforms along the plate interface shown in Figures 3b and S3). The Incorporated Research Institutions for Seismology networks (http://ds.iris.edu/wilber3/find_event) recorded these waveforms. Relocation was carried out with the Seisan package [*Havskov and Ottemöller*, 2000] by hand-picking of *P* and *S* travel times, using the waveforms recorded by the global teleseismic stations at a distance of 0°–40° of the source without a restriction in the azimuth. The 95% relocated aftershocks are lying in the megathrust ±10 km with average error 7.00 km and standard deviation 2.05 km according to the velocity model of the International Association of the Seismology and Physics of the Earth's Interior (IASPEI91) The relocated aftershocks along the megathrust with the vertical errors are provided in Figures 3b and S3. The cumulative seismic moment released by these aftershocks was $1.98 \times 10^{20}$ Nm (shown as three profiles in Figure S5). By comparing this with the geodetically estimated postseismic moment released, we can conclude that ~53% of the postseismic afterslip occurred through aseismic processes.

### 4.3. Interseismic Coupling (ISC) and Slip Deficit Rate

Previous great earthquakes that have struck this region are the $M_w > 8.5$, 1730 earthquake, which overlapped with the rupture region of the $M_w$ 8.3, 2015 event; the $M_s$ 8.4, 1906 Valparaiso earthquake [*Okal*, 2005]; and the northern portion of the $M_w$ 8.8, 2010 Maule rupture [*Vigny et al.*, 2011]. Since 1730 and 2015, ~18 m of slip deficit can accumulate at the plate interface by considering convergence rate of 6.6 cm/yr and 100% locking. However, the present estimation of locking (considered as long-term) in the region of 2015 earthquake is 65% in average; it might have accumulated ~12 m of slip deficit since 1730. It is likely that the 1880 and 1943 earthquakes could have slipped ~4–5 m in an average. Accounting the slip released during the succession of these three earthquakes (1880, 1943, and 2015), it is possible to conclude that most part of the slip deficit since 1730 has been released. The remaining slip deficit might have been released through aseismic processes as slow slip events or aseismic postseismic processes. This process could be linked to the observed swarms activity of 1997 in this region [*Lemoine et al.*, 2001], shown in Figure 1. Likewise, the same seismic activity was recently observed in Peru and Ecuador [*Vallée et al.*, 2013; *Chlieh et al.*, 2014; *Villegas-Lanza et al.*, 2016].

In Figure 4, we compare the latitudinal variations of the coseismic, postseismic, and interseismic moments. The coseismic moment released peaks at 31°S. A consistent peak appears in the interseismic moment deficit rate determined from interseismic GPS data collected before the earthquake (see inset in Figure 4). Moreover, between latitudes 30°S and 31°S, the latitudinal variation of the coseismic moment and the interseismic moment deficit rate follow a very similar decay pattern. We have also compared the modeled coseismic slip with published ISC models of *Métois et al.* [2016] and *Tilmann et al.* [2016] (shown in Figure 3c). The maximum average coseismic slip is confined in the highly coupled zone in the Illapel region. At 30°S, the afterslip distribution in the region of CFZ subducts in the northern part of the rupture,

which hosted less aftershocks but significant afterslip. This observed afterslip dominated the high aseismic slip in this region. The ISC model suggests low coupling in the region where the CFZ subducts. This indicates that the subduction of this fracture zone favors creeping at the plate interface and may act as a barrier during large seismic rupture propagation. As all historical great earthquakes stopped at this feature, the CFZ could be considered as a persistent and strong barrier. Between latitudes 31°S and 32°S, the ISC model suggests relatively high coupling in the southern part of the 2015 rupture region. One possibility is that this region broke before, during the 1880 and/or 1943 events; another possibility is that the $M_s$ 8.4, 1906 rupture overlaps with the southern rupture of the 2015 Illapel earthquake, jumping then the JFR as it did during the great $M_w > 8.5$, 1730 Valparaiso earthquake. This suggests that the JFR acts as a weak barrier that worked efficiently during the 2015 event. The moment deficit rate integrated over the 2015 Illapel rupture region and computed from the model of *Tilmann et al.* [2016] indicates a cumulative moment deficit rate of $2.8 \times 10^{18}$ Nm/yr. This rate would suggest a return period of 120 years for a characteristic $M_w$ 8.3 seismic event.

## 5. Conclusion

The Illapel earthquake ruptured a segment about 200 km along-strike, with up to 8 m slip at 20 km depth updip. The rupture was characterized by a deep propagation of the coseismic slip below the central part of the rupture, reaching up to 40 km deep downdip. We studied the postseismic phase by using GPS data of 43 days after the main shock from a local network of 13 cGPS stations. From these results, we inferred that the Illapel earthquake triggered aseismic frictional afterslip on two patches adjacent to the deep coseismic slip region. The contribution of the seismic and aseismic slip during this postseismic 43 days window probably follows the average locking degree of this region. The shallow afterslip patch (A) overlaps the coseismic slip region; it may be due to the fluid migration downdip of the maximum coseismic slip. The coseismic slip and afterslip are confined in a region, along-strike where the CFZ and JFR enter in the trench. The CFZ is the region that has been characterized by low ISC [*Métois et al.*, 2012, 2016; *Tilmann et al.*, 2016] and is suspected to be a persistent and a barrier to seismic rupture propagation, bounding the extent of past large ($M_s > 7.5$) earthquakes in 1922, 1943, and 1880 and great ($M_w > 8.5$) earthquakes in 1730 and 2015. The subducting seamount along the JFR seems to be a southern boundary of the Illapel earthquake in 2015. It may be possible that this ridge may have behaved as a weak zone for the last two earthquakes in 1880 and 1943 in the region. This study facilitates resolving the intricacies pertaining to account the aseismic slip during the afterslip, which may be an important constituent of the postseismic phase.

## References

Altamimi, Z., X. Collilieux, and L. Métivier (2011), ITRF2008: An improved solution of the International Terrestrial Reference Frame, *J. Geodesy*, *85*(8), 457–473.

Beck, S., S. Barrientos, E. Kausel, and M. Reyes (1998), Source characteristics of historic earthquakes along the central Chile subduction, *J. South Am. Earth Sci.*, *11*(2), 115–129.

Béjar-Pizarro, M., A. Socquet, R. Armijo, D. Carrizo, J. Genrich, and M. Simons (2013), Andean structural control on interseismic coupling in the North Chile subduction zone, *Nat. Geosci.*, *6*(6), 462–467.

Bilek, S. L., S. Y. Schwartz, and H. R. DeShon (2003), Control of seafloor roughness on earthquake rupture behavior, *Geology*, *31*(5), 455–458.

Chlieh, M., J. P. Avouac, K. Sieh, D. H. Natawidjaja, and J. Galetzka (2008), Heterogeneous coupling of the Sumatran megathrust constrained by geodetic and paleogeodetic measurements, *J. Geophys. Res.*, *113*, B05305, doi:10.1029/2007JB004981.

Chlieh, M., H. Perfettini, H. Tavera, J. P. Avouac, D. Remy, J. M. Nocquet, F. Rolandone, F. Bondoux, G. Gabalda, and S. Bonvalot (2011), Interseismic coupling and seismic potential along the Central Andes subduction zone, *J. Geophys. Res.*, *116*, B12405, doi:10.1029/2010JB008166.

Chlieh, M., et al. (2014), Distribution of discrete seismic asperities and aseismic slip along the Ecuadorian megathrust, *Earth Planet. Sci. Lett.*, *400*, 292–301.

Comte, D., A. Eisenberg, E. Lorca, M. Pardo, L. Ponce, R. Saragoni, S. K. Singh, and G. Suárez (1986), The 1985 central Chile earthquake: A repeat of previous great earthquakes in the region?, *Science*, *233*(4762), 449–453.

Dow, J. M., R. E. Neilan, and C. Rizos (2009), The international GNSS service in a changing landscape of global navigation saltellite systems, *J. Geodesy*, *83*(3–4), 191–198.

Duan, B. (2012), Dynamic rupture of the 2011 Mw 9.0 Tohoku-Oki earthquake: Roles of a possible subducting seamount, *J. Geophys. Res.*, *117*, B05311, doi:10.1029/2011JB009124.

Grandin, R., E. Klein, M. Métois, and C. Vigny (2016), Three-dimensional displacement field of the 2015 Mw8. 3 Illapel earthquake (Chile) from across-and along-track Sentinel-1 TOPS interferometry, *Geophys. Res. Lett.*, *43*, 2552–2561, doi:10.1002/2016GL067954.

Haberland, C., A. Rietbrock, D. Lange, K. Bataille, and T. Dahm (2009), Structure of the seismogenic zone of the southcentral Chilean margin revealed by local earthquake traveltime tomography, *J. Geophys. Res.*, *114*, B01317, doi:10.1029/2008JB005802.

Hansen, P. C. (1992), Analysis of discrete ill-posed problems by means of the L-curve, *SIAM Rev.*, *34*(4), 561–580.

Hansen, P. C., and D. P. O'Leary (1993), The use of the L-curve in the regularization of discrete ill-posed problems, *SIAM J. Sci. Comput.*, *14*(6), 1487–1503.

Havskov, J., and L. Ottemöller (2000), SEISAN earthquake analysis software, *Seismol. Res. Lett.*, *70*, 532–534.

Hayes, G. P., D. J. Wald, and R. L. Johnson (2012), Slab1.0: A three-dimensional model of global subduction zone geometries, *J. Geophys. Res.*, *117*, B01302, doi:10.1029/2011JB008524.

Heidarzadeh, M., S. Murotani, K. Satake, T. Ishibe, and A. R. Gusman (2016), Source model of the 16 September 2015 Illapel, Chile Mw 8.4 earthquake based on teleseismic and tsunami data, *Geophys. Res. Lett.*, *43*, 643–650, doi:10.1002/2015GL067297.

Henstock, T. J., L. C. McNeill, J. M. Bull, B. J. Cook, S. P. Gulick, J. A. Austin, H. Permana, and Y. S. Djajadihardja (2016), Downgoing plate topography stopped rupture in the AD 2005 Sumatra earthquake, *Geology*, *44*(1), 71–74.

Herring, T. A., R. W. King, and S. C. McClusky (2002), *GLOBK: Global Kalman Filter VLBI and GPS Analysis Program Version 10.0*, MIT, Cambridge, Mass.

Hsu, Y. J., M. Simons, J. P. Avouac, J. Galetzka, K. Sieh, M. Chlieh, D. Natawidjaja, L. Prawirodirdjo, and Y. Bock (2006), Frictional afterslip following the 2005 Nias-Simeulue earthquake, Sumatra, *Science*, *312*(5782), 1921–1926.

Johnson, K. M., J. I. Fukuda, and P. Segall (2012), Challenging the rate-state asperity model: Afterslip following the 2011 M9 Tohoku-oki, Japan, earthquake, *Geophys. Res. Lett.*, *39*, L20302, doi:10.1029/2012GL052901.

King, R. W., and Y. Bock (2002), *Documentation for the GAMIT GPS Analysis Software, Release 10.0*, MIT, Cambridge, Mass.

Kositsky, A. P., and J. P. Avouac (2010), Inverting geodetic time series with a Principal Component Analysis-based Inversion Method (PCAIM), *J. Geophys. Res.*, *115*, B03401, doi:10.1029/2009JB006535.

Lange, D., J. Geersen, S. Barrientos, M. Moreno, I. Grevemeyer, E. Contreras-Reyes, and H. Kopp (2016), Aftershock seismicity and tectonic setting of the 16 September 2015 Mw 8.3 Illapel earthquake, Central Chile, *Geophys. J. Int.*, *206*, 1424–1430.

Lay, T., H. Kanamori, and L. Ruff (1982), The asperity model and the nature of large subduction zone earthquakes, *Earthquake Prediction Res.*, *1*, 3–71.

Lee, S. J., T. Y. Yeh, T. C. Lin, Y. Y. Lin, T. R. A. Song, and B. S. Huang (2016), Two-stage composite megathrust rupture of the 2015 Mw8. 4 Illapel, Chile, earthquake identified by spectral-element inversion of teleseismic waves, *Geophys. Res. Lett.*, *43*, 4979–4985, doi:10.1002/2016GL068843.

Lemoine, A., R. Madariaga, and J. Campos (2001), Evidence for earthquake interaction in Central Chile: The July 1997–September 1998 sequence, *Geophys. Res. Lett.*, *28*, 2743–2746, doi:10.1029/2000GL012314.

Li, L., T. Lay, K. F. Cheung, and L. Ye (2016), Joint modeling of teleseismic and tsunami wave observations to constrain the 16 September 2015 Illapel, Mw 8.3 earthquake rupture process, *Geophys. Res. Lett.*, *43*, 4303–4312, doi:10.1002/2016GL068674.

Lomnitz, C. (2004), Major earthquakes of Chile: A historical survey, 1535–1960, *Seismol. Res. Lett.*, *75*(3), 368–378.

Loveless, J. P., and B. J. Meade (2011), Spatial correlation of interseismic coupling and coseismic rupture extent of the 2011 MW = 9.0 Tohoku-oki earthquake, *Geophys. Res. Lett.*, *38*, L17306, doi:10.1029/2011GL048561.

Loveless, J. P., and B. J. Meade (2016), Two decades of spatiotemporal variations in subduction zone coupling offshore Japan, *Earth Planet. Sci. Lett.*, *436*, 19–30.

McCaffrey, R. (2002), Crustal block rotations and plate coupling, in *Plate Boundary Zones*, Geodyn. Ser., vol. 30, pp. 100–122, AGU, Washington, D. C., doi:10.1029/GD030p0101.

Melgar, D., W. Fan, S. Riquelme, J. Geng, C. Liang, M. Fuentes, G. Vargas, R. M. Allen, P. M. Shearer, and E. J. Fielding (2016), Slip segmentation and slow rupture to the trench during the 2015, Mw8. 3 Illapel, Chile earthquake, *Geophys. Res. Lett.*, *43*, 961–966, doi:10.1002/2015GL067369.

Métois, M., A. Socquet, and C. Vigny (2012), Interseismic coupling, segmentation and mechanical behavior of the central Chile subduction zone, *J. Geophys. Res.*, *117*, B03406, doi:10.1029/2011JB008736.

Métois, M., C. Vigny, A. Socquet, A. Delorme, S. Morvan, I. Ortega, and C. M. Valderas-Bermejo (2014), GPS-derived interseismic coupling on the subduction and seismic hazards in the Atacama region, Chile, *Geophys. J. Int.*, *196*(2), 644–655.

Métois, M., C. Vigny, and A. Socquet (2016), Interseismic coupling, megathrust earthquakes and seismic swarms along the Chilean subduction zone (38°–18°S), *Pure Appl. Geophys.*, *173*(5), 1431–1449.

Mochizuki, K., T. Yamada, M. Shinohara, Y. Yamanaka, and T. Kanazawa (2008), Weak interplate coupling by seamounts and repeating M ~ 7 earthquakes, *Science*, *321*(5893), 1194–1197.

Moreno, M., M. Rosenau, and O. Oncken (2010), 2010 Maule earthquake slip correlates with pre-seismic locking of Andean subduction zone, *Nature*, *467*(7312), 198–202.

Moreno, M., et al. (2012), Toward understanding tectonic control on the Mw 8.8 2010 Maule Chile earthquake, *Earth Planet. Sci. Lett.*, *321*, 152–165.

Moreno, M., C. Haberland, O. Oncken, A. Rietbrock, S. Angiboust, and O. Heidbach (2014), Locking of the Chile subduction zone controlled by fluid pressure before the 2010 earthquake, *Nat. Geosci.*, *7*(4), 292–296.

Müller, R. D., W. R. Roest, J. Y. Royer, L. M. Gahagan, and J. G. Sclater (1997), Digital isochrons of the world's ocean floor, *J. Geophys. Res.*, *102*, 3211–3214, doi:10.1029/96JB01781.

Okal, E. A. (2005), A re-evaluation of the great Aleutian and Chilean earthquakes of 1906 August 17, *Geophys. J. Int.*, *161*(2), 268–282.

Okuwaki, R., Y. Yagi, R. Aránguiz, J. González, and G. González (2016), Rupture process during the 2015 Illapel, Chile earthquake: Zigzag-along-dip rupture episodes, *Pure Appl. Geophys.*, *173*(5), 1011–1020.

Perfettini, H., and J. P. Avouac (2004), Postseismic relaxation driven by brittle creep: A possible mechanism to reconcile geodetic measurements and the decay rate of aftershocks, application to the Chi-Chi earthquake, Taiwan, *J. Geophys. Res.*, *109*, B02304, doi:10.1029/2003JB002488.

Perfettini, H., and J. P. Avouac (2014), The seismic cycle in the area of the 2011 Mw9. 0 Tohoku-Oki earthquake, *J. Geophys. Res. Solid Earth*, *119*, 4469–4515.

Perfettini, H., et al. (2010), Seismic and aseismic slip on the Central Peru megathrust, *Nature*, *465*(7294), 78–81.

Ruiz, S., et al. (2016), The seismic sequence of the 16 September 2015 Mw 8.3 Illapel, Chile, earthquake, *Seismol. Res. Lett.*, doi:10.1785/0220150281.

Scholz, C. H., and C. Small (1997), The effect of seamount subduction on seismic coupling, *Geology*, *25*(6), 487–490.

Schurr, B., et al. (2014), Gradual unlocking of plate boundary controlled initiation of the 2014 Iquique earthquake, *Nature*, *512*(7514), 299–302.

Tilmann, F., et al. (2016), The 2015 Illapel earthquake, central Chile: A type case for a characteristic earthquake?, *Geophys. Res. Lett.*, *43*, 574–583, doi:10.1002/2015GL066963.

Udías, A., R. Madariaga, E. Buforn, D. Muñoz, and M. Ros (2012), The large Chilean historical earthquakes of 1647, 1657, 1730, and 1751 from contemporary documents, *Bull. Seismol. Soc. Am.*, *102*(4), 1639–1653.

Vallée, M., et al. (2013), Intense interface seismicity triggered by a shallow slow slip event in the Central Ecuador subduction zone, *J. Geophys. Res. Solid Earth*, *118*, 2965–2981, doi:10.1002/jgrb.50216.

Vigny, C., A. Rudloff, J. C. Ruegg, R. Madariaga, J. Campos, and M. Alvarez (2009), Upper plate deformation measured by GPS in the Coquimbo Gap, Chile, *Phys. Earth Planet. Inter.*, *175*(1), 86–95.

Vigny, C., et al. (2011), The 2010 Mw 8.8 Maule megathrust earthquake of Central Chile, monitored by GPS, *Science*, *332*(6036), 1417–1421.

Villegas-Lanza, J. C., J. M. Nocquet, F. Rolandone, M. Vallée, H. Tavera, F. Bondoux, T. Tran, X. Martin, and M. Chlieh (2016), A mixed seismic-aseismic stress release episode in the Andean subduction zone, *Nat. Geosci.*, *9*, 150–154, doi:10.1038/ngeo2620.

Wang, K., and S. L. Bilek (2011), Do subducting seamounts generate or stop large earthquakes?, *Geology*, *39*(9), 819–822.

Wessel, P., and W. H. F. Smith (1991), Free software helps map and display data, *Eos Trans. AGU*, *72*, 441–441, doi:10.1029/90EO00319.

Zhang, Y., G. Zhang, E. A. Hetland, X. Shan, S. Wen, and R. Zuo (2016), Coseismic fault slip of the September 16, 2015 Mw 8.3 Illapel, Chile earthquake estimated from InSAR data, *Pure Appl. Geophys.*, *173*(4), 1029–1038.